Mesoscale variability from a high-resolution model and from altimeter data in the North Atlantic Ocean

S. Brachet and P. Y. Le Traon

CLS Space Oceanography Division, Ramonville-St-Agne, France

C. Le Provost[1]

Laboratoire d'Etudes en Géophysique et Océanographie Spatiales, Toulouse, France

[1] The objective of the paper is to analyze the degree of realism of the Parallel Ocean Program (POP) model of the Los Alamos Laboratory using the combined TOPEX/ Poseidon and ERS-1/2 (TPERS) sea level anomaly (SLA) data sets and to present a detailed study of mesoscale characteristics in the North Atlantic. This description spans 8 years of data from 1993 to 2000. At first, we focus on the analysis of the mean eddy kinetic energy (EKE) and show that the major characteristics of mesoscale variability are realistically simulated despite an overestimation of the EKE model in the Gulf Stream region. We then describe the SLA space and timescales and propagation velocities at a resolution never achieved before. There is a high level of agreement between the model and altimeter values regarding spatial scales and propagation velocities. POP timescales are, however, significantly longer in the subtropical regions. The westward zonal propagation velocity of both the model and the observations are higher than the speed computed from standard Rossby wave theory. The effect of mean current advection on POP and TPERS propagation velocities is also clearly seen in the Labrador Current and in the Gulf Stream and its recirculations. Finally, a study of the seasonal and interannual variability of the high-frequency (HF) EKE is carried out. The model reproduces accurately most of the HF-EKE seasonal variations in the Caribbean Sea and at high latitudes despite a phase advance. A clear HF-EKE interannual variability is then evidenced. Our hypothesis is that a contraction of the subpolar and subtropical gyres due to the North Atlantic Oscillation (NAO) could explain a reduction of the eddy activity in the North Atlantic Current, in the Newfoundland basin, and in the Azores Current. In the Caribbean Sea, the interannual variability of the EKE for both POP and TPERS seems to be caused by an interannual variability of the wind stress. *INDEX TERMS:* 4520 Oceanography: Physical: Eddies and mesoscale processes; 4275 Oceanography: General: Remote sensing and electromagnetic processes (0689); *KEYWORDS:* eddy kinetic energy, North Atlantic Ocean

1. Introduction

[2] The ocean is a fundamentally turbulent system. Mesoscale variability can be observed almost anywhere, the eddy energy generally exceeding the energy of the mean flow by an order of magnitude or more. Instability processes are the principal sources of eddy energy, but in low-eddy-energy regions, fluctuating winds can be a direct forcing mechanism [e.g., *Frankignoul and Müller*, 1979]. Eddies can feed energy back to the mean flow and drive deep circulation [*Holland et al.*, 1982; *Lozier*, 1997]. Resolving mesoscale variability is thus essential to correctly simulate the dynamics of ocean circulation and the associated heat transport, even at large and climatic scales [e.g., *Wunsch*, 1999; *Roemmich and Gilson*, 2001].

[3] Over the past 20 years, major advances in mesoscale variability observation and modeling have been achieved. Satellite altimetry has provided a unique contribution to the global observation of eddy variability (see *Le Traon and Morrow* [2001] for a recent review). Since 1992, TOPEX/ Poseidon (TP) and ERS-1/2 have been flying simultaneously, providing a more detailed description of mesoscale characteristics than ever before [e.g., *Ducet et al.*, 2000; *Ducet and Le Traon*, 2001]. At the same time, eddy-resolving modeling has progressed significantly and high-resolution models have now reached a high degree of realism [*Smith et al.*, 2000]. This allows a more detailed comparison between altimeter data and models. Such comparisons are required to improve the validation of models but also to gain a further insight into mesoscale dynamics and to assist with

---

[1]Deceased 29 February 2004.
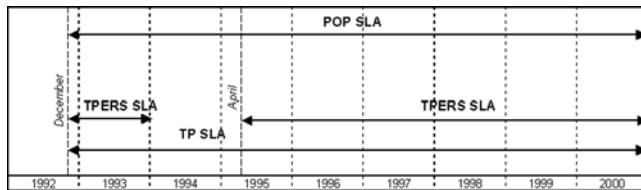
Figure 1. POP, the model, TP, the altimetric data, and TPERS, the combined TP and ERS-1/2 altimetric data. The computed sea level anomaly (SLA) is relative to a 3-year mean (January 1993 to January 1996).

the interpretation of satellite altimetry observations. They are also needed to develop effective altimeter data assimilation techniques.

[4] In the past, several studies have focused on model and altimeter data comparisons. *Stammer et al.* [1996] have shown that the eddy kinetic energy (EKE) in the POP 1/4° model simulations was 4 times lower compared to TOPEX/ Poseidon. More recently, *Smith et al.* [2000] have presented a comparison between the LANL 1/10° high-resolution model and altimeter data. They found, for the first time, an accurate agreement between model and altimetry that they mainly attributed to the improvement in model resolution. In this paper, LANL model outputs will be compared to combined altimeter data sets from TP and ERS over a longer period (8 years from December 1992 to December 2000) and a much more detailed description of the mesoscale variability will be carried out. It will include, in particular, a characterization of the space, timescales and propagation velocities of the mesoscale variability and an analysis of the EKE seasonal and interannual variations.

[5] The paper is organized as follows. Model and altimeter data are first presented in section 1. Mean EKE derived from altimetry and from the LANL model are then analyzed and compared in section 2. Section 3 compares the characteristic space and timescales of mesoscale variability as derived from altimetry and the LANL model. Propagation velocities are also derived and compared to Rossby wave theory. Finally, in section 4, the temporal evolution of the monthly EKE over the 8-year period is analyzed across the whole North Atlantic Ocean. We focus on four main areas of apparent seasonal variability: the Gulf Stream, the Caribbean Sea, the Labrador Sea, and the Irminger Sea. An attempt is made to relate the seasonal signal to the different mesoscale variability forcing mechanisms. Finally, we describe the interannual variability of the EKE by analyzing the evolution over time of the annual EKE anomalies between 1993 and 2000. Main conclusions are given in section 5.

2. Model and Altimeter Data

2.1. Data

[6] Data from both the U.S. TOPEX dual-frequency and the French Poseidon altimeters (T/P), and from the European ERS-1/2 altimeters, spanning the period from December 1992 to December 2000 are used. SLA relative to a 3-year mean (from January 1993 to January 1996) are first computed for TOPEX, Poseidon, and ERS-1/2 altimeters. Maps of SLA merging the different altimeters

are then obtained using a global space/time objective analysis method [see *Ducet et al.*, 2000]. The maps from 24 December 1993 to 24 March 1995, during the ERS-1 geodetic mission are obtained only from T/P data; see Figure 1. Maps are available every 10 days with a grid resolution of 0.25° for both latitude and longitude.

2.2. Model

[7] Eight years of model outputs (from December 1992 to December 2000) from run 13 of the Los Alamos National Laboratory (LANL) Parallel Ocean Program (POP), a level-coordinate ocean general circulation model (OGCM), are used in this study [*Smith et al.*, 2000]. The model has a 0.1° Mercator grid resolution and 40 vertical levels, thickness increasing with depth. The ocean floor topography was derived from the 1/12° ETOPO5 database from the National Geophysical Data Center. Wind-forcings are derived from the ECMWF analysis data set, and the heat flux forcing uses the seasonal climatology of *Barnier et al.* [1995]. The surface freshwater fluxes are simulated by a relaxation to the Levitus monthly salinity climatology [*Levitus*, 1982]. At the northern and southern buffer zones the temperature and salinity are restored to the seasonal values of that climatology.

[8] The study is based on model outputs of sea-surface height (SSH) with a snapshot every 3 days. To have equivalent sea level anomalies (SLA) between POP and TPERS, we compute the model anomalies using the same mean SSH $(\overline{SSH})$ (SLA = SSH $- \overline{SSH}$) as the altimetric one, i.e., from January 1993 to January 1996.

[9] Our study is limited to the North Atlantic Ocean from 9°N to 70°N, including the Gulf of Mexico and excluding the Mediterranean Sea. The Mercator grid is interpolated on a regular grid with a step of 0.1° in longitude and latitude for comparison with the 0.25° regular grid of the altimeter data.

3. Mean EKE (1995–2000)

[10] To evaluate the POP 1/10° resolution model's ability to simulate mesoscale features, the LANL EKE was first compared to the EKE derived from T/P + ERS combined maps. Such comparisons were made previously by *McClean et al.* [1997] and *Stammer et al.* [1996] over the global ocean for OGCM at a lower resolution. The EKE analysis of *Smith et al.* [2000] is extended in this paper. Errors on EKE estimations derived from T/P and ERS maps have been analyzed by *Ducet* [2000], *Ducet et al.* [2000], and *Le Traon and Dibarboure* [2002] both from simulation studies that analyzed altimeter sampling effects and from the comparison with WOCE surface drifters and current meters. These analyses showed that the EKE derived from the combined altimeter data set captures the amplitude and spatial structure of the variability well except in high-latitude regions. In these regions, the altimeter EKE is likely to be underestimated by 30% to 40% due to a high frequency and high wave number signals that cannot be mapped from altimeter data. The effect is smaller in midlatitude regions (e.g., Gulf Stream), and the underestimation there should be of about 10 to 20%. *Fratantoni* [2001] also found large differences between altimeter and drifter EKEs in high latitudes. He also noted significant positive and negative differences in the Gulf Stream region

that are likely due to drifter EKE averaging procedure and to the heterogeneous sampling by the drifter data.

[11] The zonal (U'_g) and meridional (V'_g) velocity anomalies are derived from the SLA data using the geostrophic approximation,

$$U'_g = -\frac{g}{f}\frac{\partial SLA}{\partial y}, \; V'_g = \frac{g}{f}\frac{\partial SLA}{\partial x},$$

where g is gravity and f is the Coriolis parameter. SLA gradients are calculated over a distance of $0.1 \times \cos \varphi$ (where φ is latitude) using spline functions for both satellite and model data. The variance of these velocity anomalies corresponds to the eddy kinetic energy (EKE),

$$EKE = \frac{1}{2}\left[\langle U'^2_g \rangle + \langle V'^2_g \rangle\right].$$

[12] The LANL EKE compares reasonably well to the T/P + ERS EKE. The major characteristics of mesoscale variability are realistically simulated (Figure 2): the Gulf Stream, the North Atlantic Current (NAC), the Caribbean Sea, the Loop current, the Azores Current, and areas of lower mesoscale variability.

[13] If we compare the mean amplitude of the EKE in the Gulf Stream simulated by the model and the amplitude obtained from the observations over the GS box, we find, however, that the model is higher by a factor of 2 compared to the observations (Figures 3 and 4). As explained above, we expect a slight underestimation of the altimeter EKE in the Gulf Stream region. This cannot explain, however, the observed differences. Thus they likely result from problem within the model.

[14] In Figure 5, we present the basin-wide zonal average EKE for POP and for TPERS. This figure clearly demonstrates that the path of the Gulf Stream is not far enough north for POP, as already mentioned by *Smith et al.* [2000]. A peak of variability remains around 36°N–37°N for POP and around 39°N for TPERS or drifter EKE [*Ducet et al.*, 2000; *Fratantoni*, 2001], even though the separation from the coast, near Cape Haterras, appears realistic. Besides, the area of high EKE is more expanded; this means that the GS is too turbulent in our GS box, spreading EKE too far south.

[15] In Figure 4 we present the mean zonal and meridional velocity variances of the EKE in the Gulf Stream and Gulf Stream extension for both POP and TPERS. It shows the apparent anisotropy of the Gulf Stream mesoscale variability. The broad outlines of this anisotropy are a persistent double blade in the zonal velocity variance at 35°N–37°N, a decrease (increase) of the zonal (meridional) velocity variance after 303°E [*Ducet and Le Traon*, 2001]. In the POP model, these characteristics are not accurately represented; the decrease occurs for both zonal and meridional variances and is too pronounced for the zonal variance. The model GS variability is too large along its path from Cape Hatteras and the Corner Rise Seamounts (CRSM), and its extension to the east is blocked by the CRSM. In the T/P-ERS observations, the GS EKE has a more zonal structure, allowing the GS to penetrate more efficiently eastward of the CRSM barrier, which destabilizes the flow and induces a more intense meridional EKE
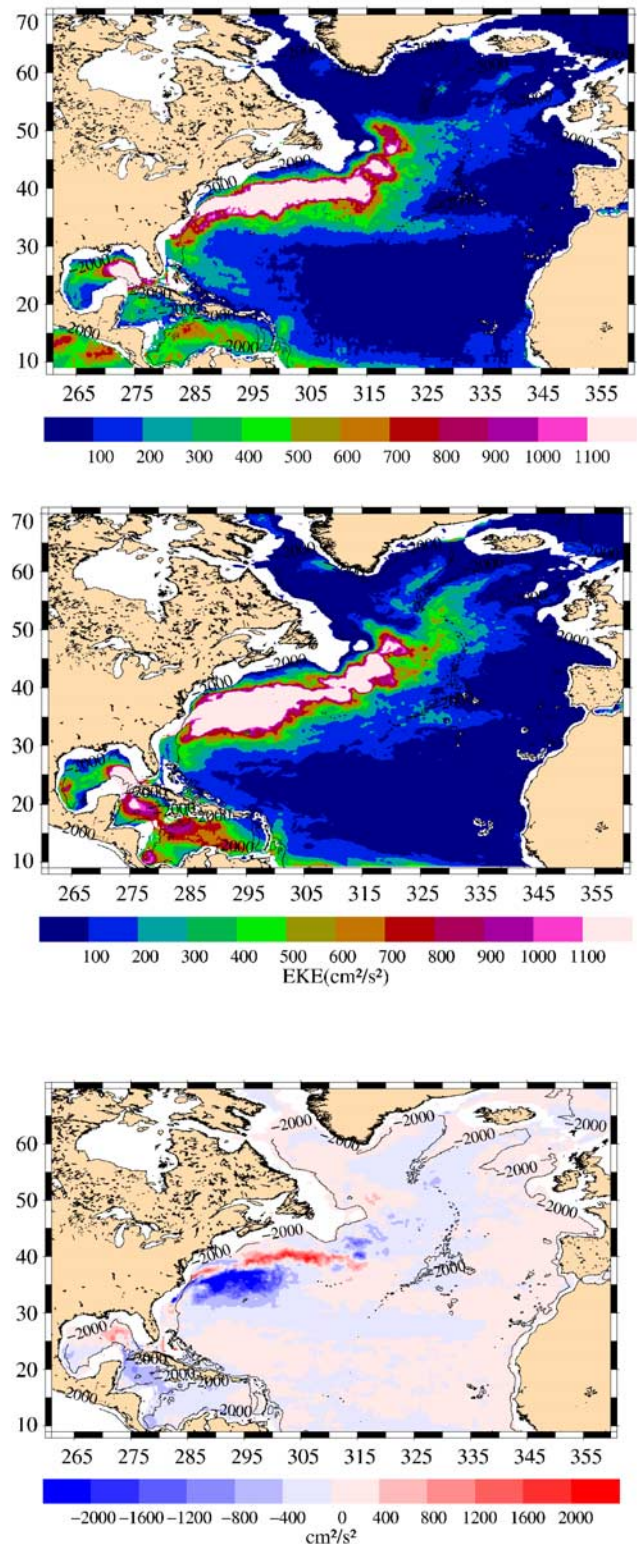
Figure 2. Mean EKE (1995–2000) in the North Atlantic (top) TPERS and (middle) POP, in cm^2/s^2. The bathymetry corresponds to a 3500 m depth. (bottom) Difference between TPERS and POP EKE.
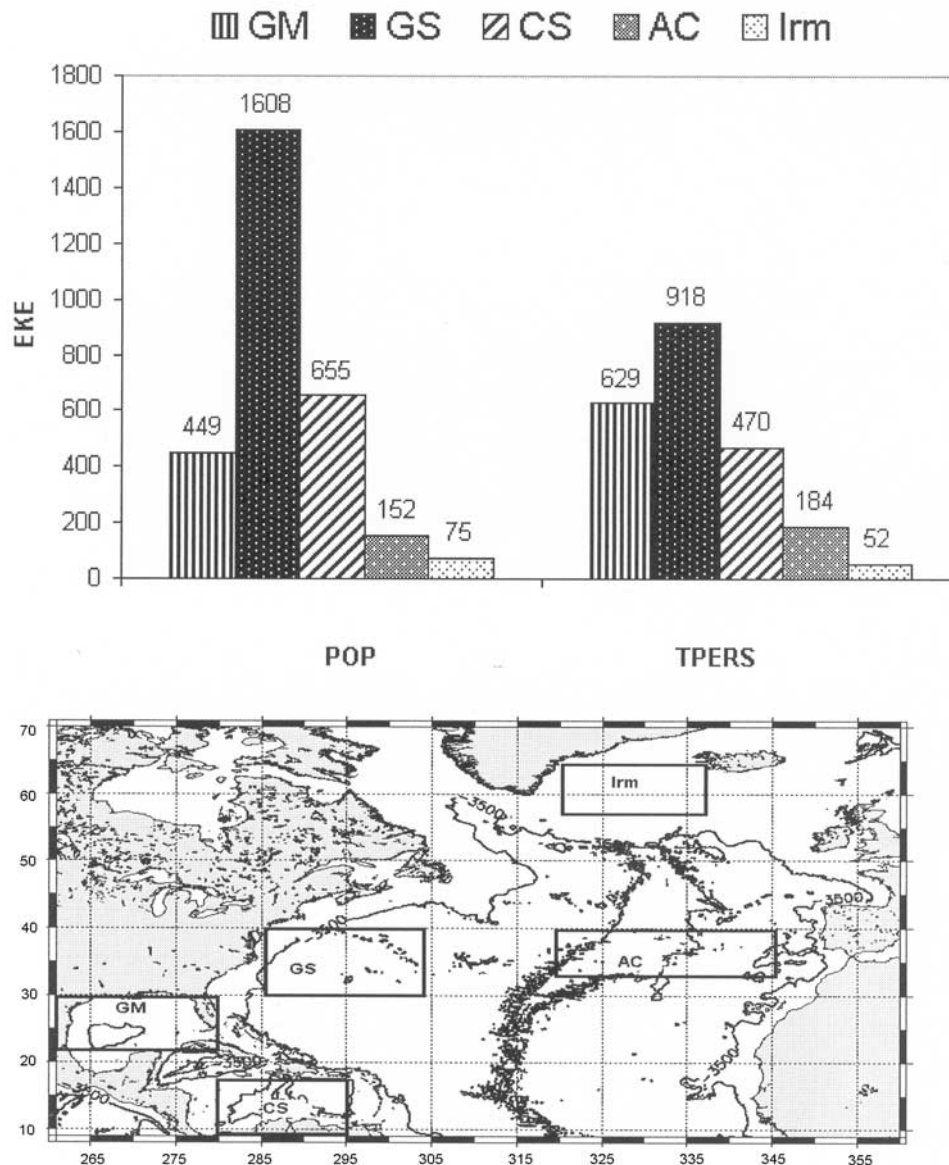
Figure 3. Spatial average of EKE in cm²/s² in the Gulf of Mexico (GM), Gulf Stream (GS), Azores Current (AC), Caribbean Sea (CS), and Irminger Sea (Irm).

activity. Nevertheless, the model accurately describes the general tendency of mesoscale variability to be more zonal between 285°E and 296°E. One explanation could be the grid resolution. *Hurlburt and Hogan* [2000] tested the variation of the Gulf Stream width with the resolution of the model. They found that at a resolution of 1/64° the width of the Gulf Stream decreases compared to simulations at lower resolution.

[16] The GS extension branches into two currents east of 312°E, the North Atlantic Current (NAC) and a southeastward branch, which is one of the origins of the Azores Current (AC). The presence of the drift of the NAC, a northwestward branch of the Gulf Stream extension, which occurs just past the Grand Banks, is a major feature of the circulation of the North Atlantic. The presence of this branch in the POP model represents a significant improvement over previous model simulations. The AC is present in

the model, correctly positioned and accurately directed toward the Strait of Gibraltar. The amplitude of the EKE is approximately the same as in the data (Figure 3). A slight shift can be noticed between POP and TPERS.

[17] In Figure 2, the variability at high latitudes is at similar geographic locations for the model and the data. The major difference at these latitudes is the amplitude of the EKE. It can be seen in the histogram (Figure 3) that the amplitude of the EKE in the Irminger sea is 30% higher for POP than for TPERS. The sampling and objective analysis are the main reason for this low signal for TPERS. *Ducet* [2000] and *Le Traon and Dibarboure* [2002] showed that up to 40% of the signal may be missed at these latitudes because the high-latitude variability is poorly resolved by the combination of TP and ERS measurements.

[18] At tropical latitudes, the variability associated with the North Brazil Current (NBC) comes from the NBC
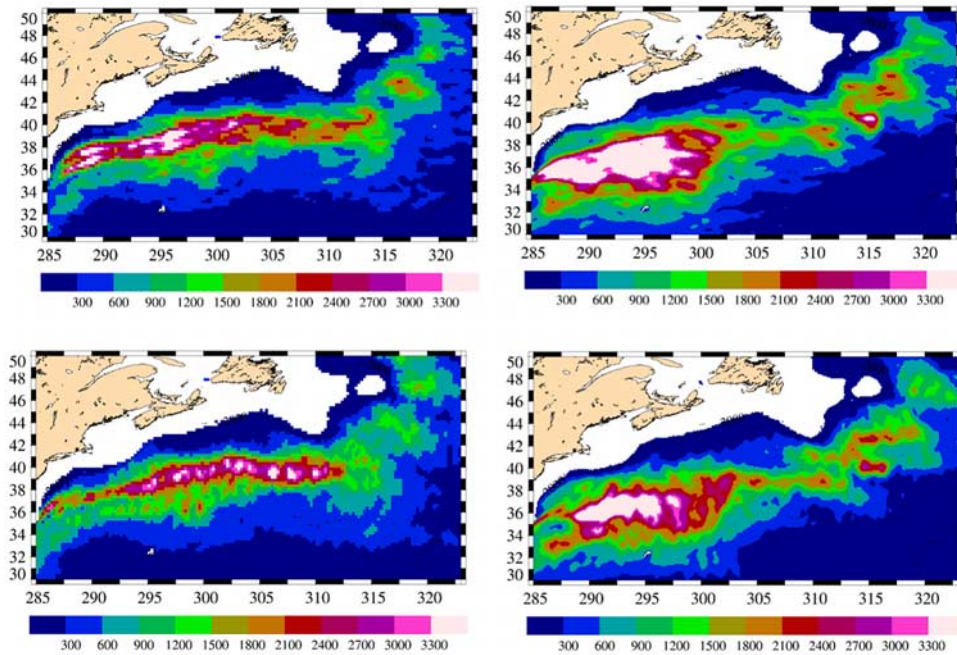
Figure 4. (top) $\langle U'^2 \rangle$ and (bottom) $\langle V'^2 \rangle$ in the Gulf Stream for (left) TPERS and (right) POP. Unit is cm^2/s^2.

retroflection into the North Equatorial Countercurrent (NECC) in the summer [*Didden and Schott*, 1993; *Larnicol*, 1998]. These structures, formed at 5°N–8°N, 310°E, are propagated to the Caribbean Sea (CS). Figure 2 suggests that the model simulates a higher variability in the CS. Several mechanisms act to limit this variability that are apparently not properly taken into account within the model. *Barnier et al.* [2001] explain, in particular, that the presence of islands reduces the propagation of eddies, as can be observed for TPERS. In the model, eddies seem to propagate across the islands. Another point is the influence of the bathymetry. The friction at the bottom causes a dissipation of the energy of eddies in the CS [*Barnier et al.*, 2001]. The sharp features could be not sufficiently taken into account as suggested by *Smith et al.* [2000]; as a consequence, the bottom friction may be too low in the model and the energy may not be dissipated enough.

[19] In the Gulf of Mexico the EKE geographical distribution is similar for the model and for the data. However, the variability of the Loop Current (LC) is stronger in the data than in the model, by about 20%. Other domains differ, like in the Cape Verde Basin, 335°E, 15°N, where the mesoscale variability is present only in the observations. Close to the African coast, variability associated with upwelling is observed in TPERS and is not well represented by the model.

4. Space Scales and Timescales and Propagation Velocities

4.1. Method

[20] A 4-year time series (1996–1999, corresponding to the entire period covered by the combined data) of sea level anomalies (SLA) (10 days maps at 0.25° × 0.25° resolution) is used to evaluate the space-timescales of POP and

TPERS in the North Atlantic. The different parameters studied are: Lx and Ly, the zonal and meridional eddy spatial scales; T, the "propagative" (i.e., in a referential moving at Cpx and Cpy velocities) timescale; and Cpx and
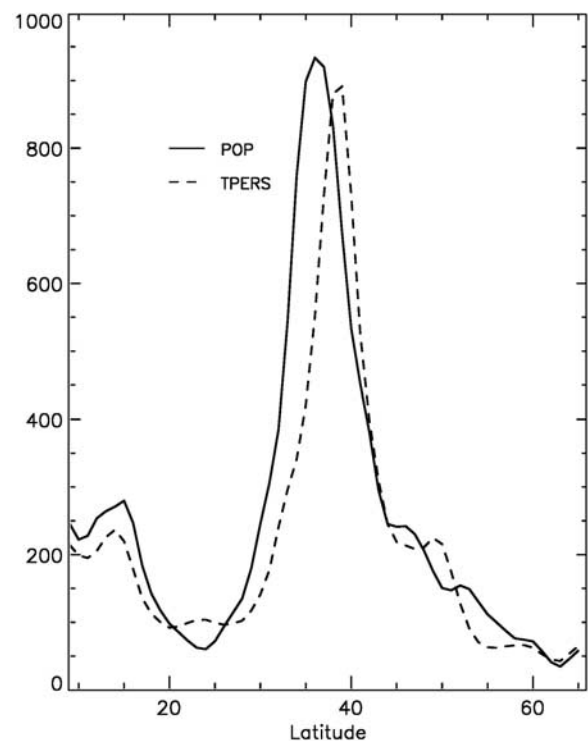
Figure 5. Basin-wide average EKE for POP (solid line) and for TPERS (dotted line). EKE is in cm^2/s^2.

Cpy, the zonal and meridional propagation speeds. *Jacobs et al.* [2001] computed these variables in the global ocean using TPERS data on a 2° latitude-longitude grid. Here we focus on the North Atlantic Ocean on a 2°longitude × 1°latitude grid.

[21] At first, we compute a discrete correlation function from POP and TPERS. A space-time domain is defined to optimize the computing of these different parameters. A 15-day temporal radius is chosen that corresponds to four consecutive grids (30 days) and, to focus on mesoscale signals, the spatial radius R is chosen to vary from 350 km at low latitudes to 150 km at 60°N. This spatial radius depends on latitude and corresponds to the typical spatial scales of SLA used by *Ducet et al.* [2000].

[22] The covariance functions are computed between each pair of points $(\vec{X}_i, t_i)$ and $(\vec{X}_j, t_j)$ with $t_i - t_j < 30$ days and $\vec{X}_i - \vec{X}_j < R$ km, inside the defined time-space domain. The covariance functions are then normalized by the variance and fitted to obtain the following space-time autocorrelation function C_{mod} (dx, dy, dt) (dx and dy are the zonal and meridional spatial lags, and dt is the time lag):

$$C_{mod}(dx, dy, dt) = \left[1 + ar + \frac{1}{6}(ar)^2 - \frac{1}{6}(ar)^3\right]e^{-ar}e^{-\left(\frac{dt}{T}\right)^2}$$

where $r = \sqrt{\left(\frac{dx - C_{px}dt}{L_x}\right)^2 + \left(\frac{dy - C_{py}dt}{L_y}\right)^2}$ and a = 3.337.

[23] Figure 6 summarizes the method described above. On the left-hand side, the observed correlation function is shown for time lags of 0, 10, 20, and 30 days (from top to bottom). The fitted correlation function is shown on the right-hand side.

[24] This covariance model is able to take into account the presence of zonal and meridional propagation in the SLA. This model differs from that of *Kuragano and Kamachi* [2000] by including a polynomial that allows us to fit zero-crossing autocorrelation functions and by the absence of crossed terms in dx and dy so that the major axes of the ellipsoid will be north-south and east-west. Crossed terms in dx (or dy) and dt also only appear through our definition of r and propagation speed.

[25] The geographical variations of Lx, Ly, T, Cpx, Cpy for TPERS (left) and POP (right) are shown in Figure 7. A Loess low-pass filter [*Schlax and Chelton*, 1992] was applied to obtain a smoother signal, and all the data that correspond to a depth of less than 500 m have been removed to avoid incoherent coastal signal noise.

4.2. Space Scales and Timescales

[26] Figures 7a and 7b correspond to the zonal and meridional space scales for TPERS at left and POP at right. At left, in Figures 7a and 7b, the observed spatial scale maximum of 250 km is localized at low latitudes in the tropical North Atlantic Ocean and in the Caribbean Sea. The space scale minimum of 90 km covers a large part of the subpolar gyre (45°N–65°N) particularly in the east. At right, Figures 7a and 7b, the model spatial scales are very similar to the altimetric ones. The major difference for Lx and Ly is that the minimum is lower in the model by about 20–40 km at latitudes higher than 52°N. As previously noted, the high-latitude regions are not sampled enough by altimetry and this is likely to result in an overestimation of spatial scales. For the meridional spatial scales, Figure 7b, it

can be noticed that the model values are globally lower than TPERS but the model represents accurately all the local characteristics: close to the Africa coast, the Guyana coast, in the Caribbean Sea, close to the Peninsula of Yucatan, in the Florida Strait, and along the major currents in the subpolar gyre, the Labrador Current and Irminger Current.

[27] In Figure 8 the spatial scales in the North Atlantic (280°E–360°E, 9°N–69°N) are averaged over the basin larger and compared to the Rossby radius of deformation from *Chelton et al.* [1998] for the North Atlantic Ocean. The general tendency of a decrease with increasing latitudes for both Lx and Ly is expected because of the decrease of the first baroclinic Rossby radius of deformation [*Le Traon*, 1991; *Stammer*, 1997; *Le Traon and Morrow*, 2001]. The rise in the high latitudes (60°N and above) is most likely due to the large contribution of the large-scale barotropic response of the ocean to wind-forcing [e.g., *Chao and Fu*, 1995].

[28] In Figure 7c, the propagative timescales are represented. A major difference between the model and the data can be noted. The model timescales are higher than in the observations at almost all latitudes (lower than 40°N). *Ducet* [2000] found a similar result for time decorrelation scales (i.e., nonpropagative timescales). Nevertheless, it shows the same variations with latitudes as in TPERS data. From 45°N to 67°N, timescales are identical for both model and data. The major bias is in the east basin at latitudes between 20°N and 45°N, where larger timescales are found in the model. The lifetime of eddies or waves is probably too long in the model, with not enough damping through mixing. It has been suggested recently that mixed layer dynamics (buoyancy forcing) may explain the damping of waves [*Thompson et al.*, 2002]. It should be recalled that the POP model has a very simple approach to vertical mixing in the mixed layer based on convective adjustment and an explicit vertical mixing parameterization [*Pacanowski and Philander*, 1981].

4.3. Propagation Speeds
### 4.3.1. Comparison Between POP and TPERS

[29] The POP and TPERS zonal (cpx) and meridional (cpy) propagation velocities also agree quite well. Not only is the general tendency well featured, but also the local propagation characteristics are well represented in both observation and model estimations. In particular, the contribution of the advection of the major currents to the propagation velocities is clearly evidenced in the Gulf Stream (northward propagation then eastern propagation) and its recirculation branches (westward propagations), the Labrador Current (southward propagation) and more generally the subpolar gyre. For the meridional propagation velocity, the model appears reasonably correct because the speeds range between 1 and −1 km per day, which are very low. The most remarkable difference is at 55°N to 67°N, where the model velocities are too fast. However, the directions and variations are consistent with the TPERS observations. The northward propagation of eddies in the Caribbean Sea (propagation of eddies generated from the retroflexion of the North Equatorial Counter Current) is also clearly shown.

[30] The scatterplot between POP and TPERS zonal propagation velocities (Figure 9) quantifies the excellent
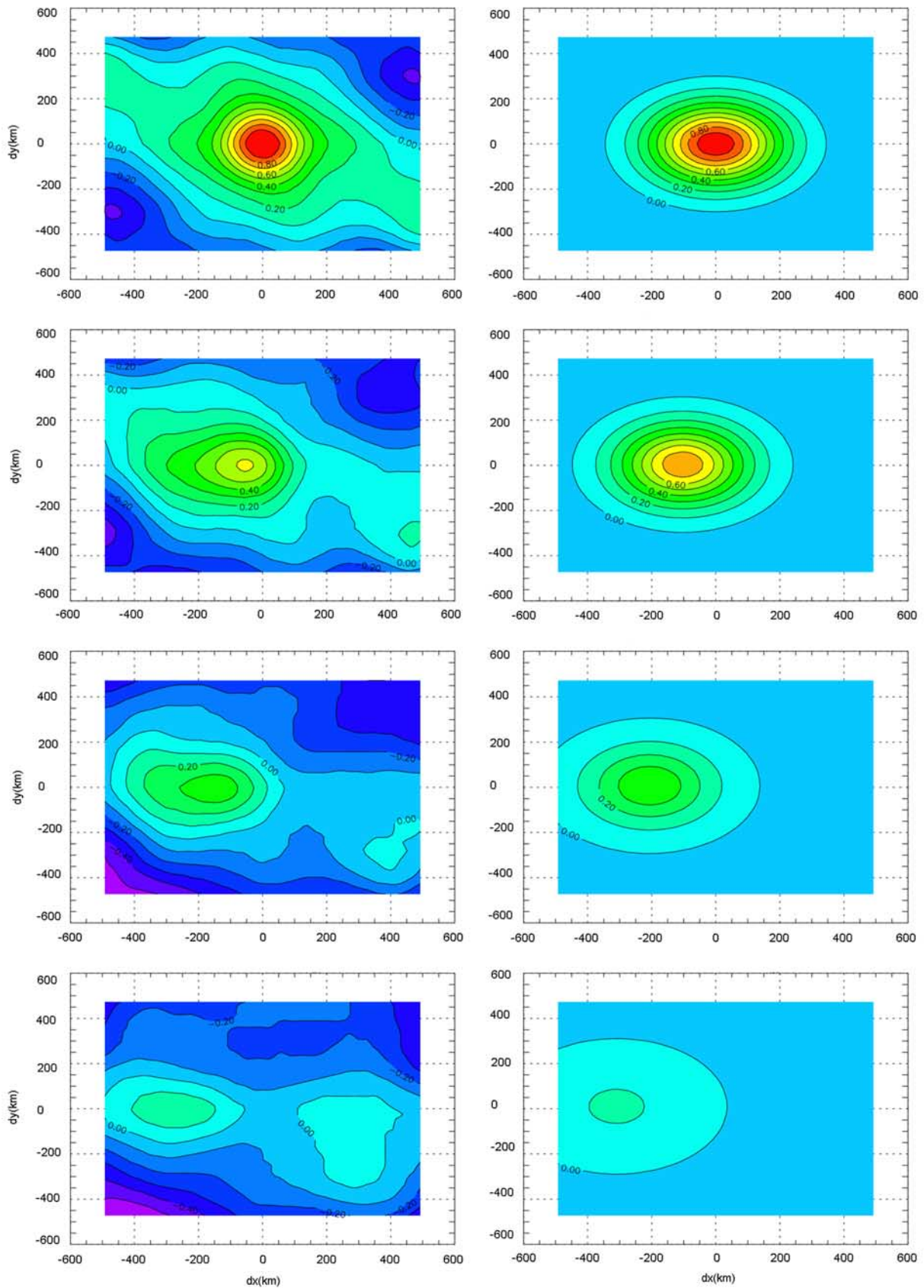
Figure 6. Example of (left) observed and (right) fitted correlation function for a given point. The correlation function is shown for time lags of (top to bottom) 0, 10, 20, and 30 days. The fitted correlation function is shown on the right-hand side.
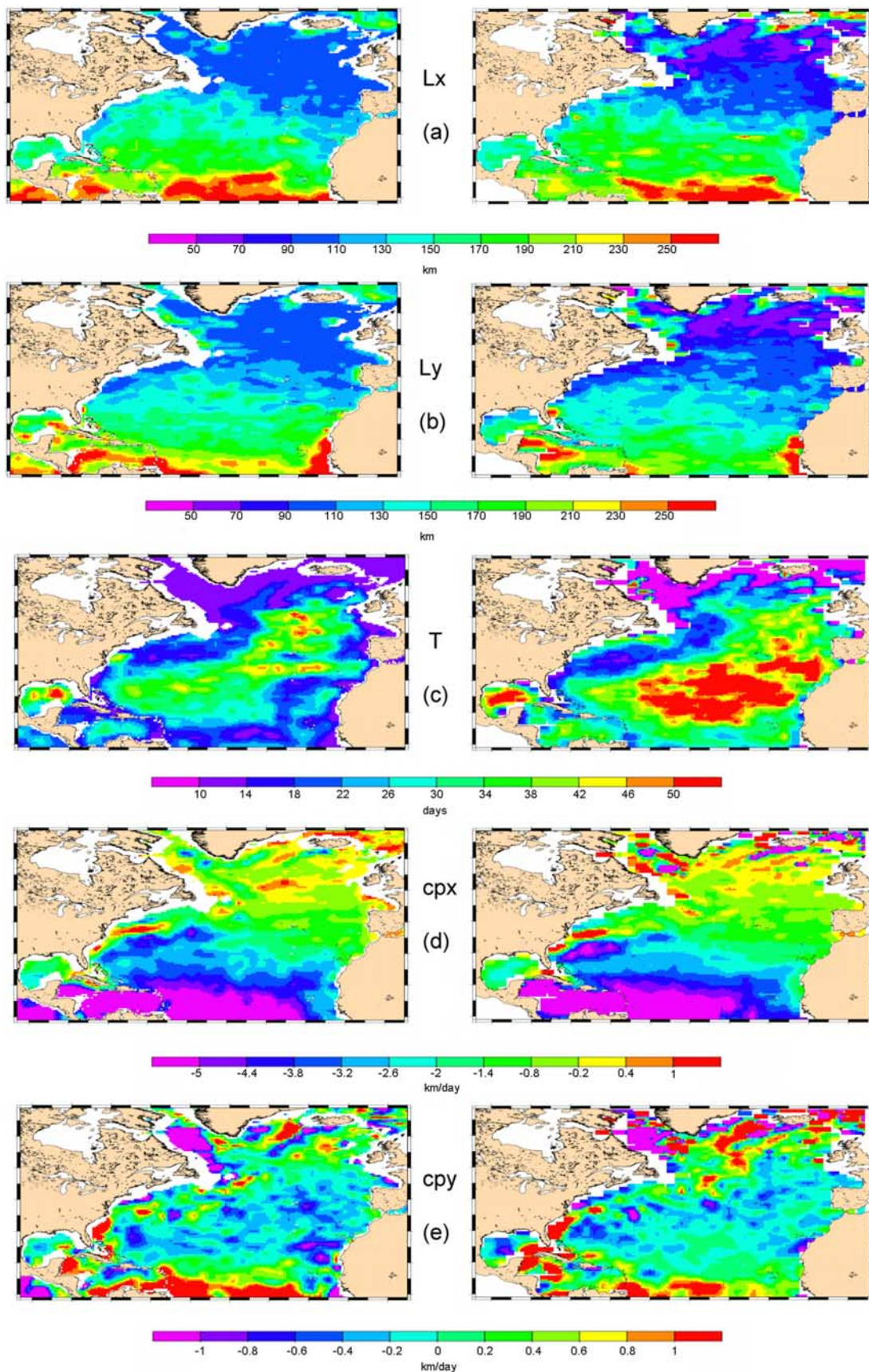
Figure 7. (a) Lx and (b) Ly, the zonal and meridional eddy spatial scales (km), (c) T, the propagation timescale of correlations (days), and (d) Cpx and (e) Cpy, the zonal and meridional propagation speeds (km per day) for (left) TPERS and (right) POP.
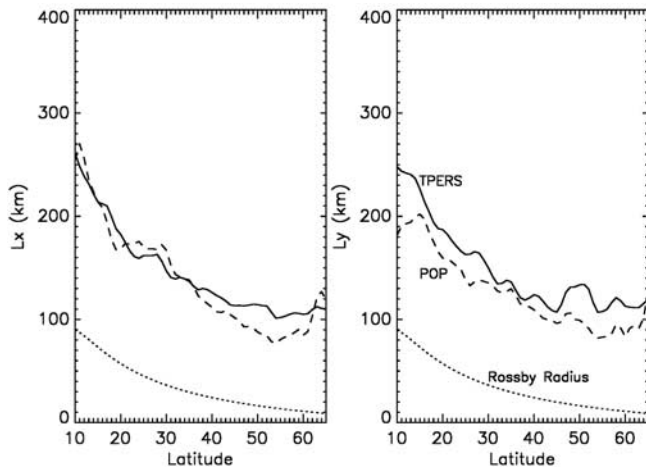
Figure 8. Zonal averages in the North Atlantic for POP (dashed line) and TPERS (solid line), for (left) the zonal lengthscale (km) and (right) the meridional lengthscale (km). The theoretical Rossby radius of deformation is shown as the dotted line.

agreement between the two estimations. The regression line is very close to 1.

4.3.2. Comparison With Linear Rossby Wave Theory

[31] Although eddy dynamics are dominated by nonlinear effects, eddy propagation velocities are related to linear Rossby wave propagation velocity. *McWilliams and Flierl* [1979] showed, for example, that a vortex moves westward at the greatest linear Rossby wave speed [see also *Nof*, 1981; *Cushman-Roisin et al.*, 1990]. It is thus instructive to compare our propagation velocities to standard Rossby wave propagation velocities.

[32] *Chelton and Schlax* [1996] first pointed out a discrepancy between the zonal propagation speed observed by TP and linear Rossby wave theory. Their zonal propagation speed was systematically higher than the theoretical long planetary waves. *Killworth et al.* [1997] noted that the presence of the mean flow modifies the potential vorticity gradient and then affects the propagation speeds. *Zang and Wunsch* [1999] analyzed, with TP data, the problem differently, by separating different frequency and wave number bands. They also found some motions with a propagation speed higher than obtained using linear theory. Using TPERS data, *Jacobs et al.* [2001] found, however, that eddies propagate at speeds close to standard Rossby wave theoretical values. The question of the existence of a discrepancy between the observed Cpx and the theoretical Cpx is still open.

[33] According to linear quasi-geostrophic theory, on a β-plane, waves generated by anomalies propagate westward [e.g., *Pedlosky*, 1987]. The propagation speeds C_{nx} of these waves is given by $C_{nx} = \frac{-\beta}{k^2 + l^2 + \lambda_n^{-2}}$, where λ_n is the Rossby radius deformation, k and l are the wave numbers, and β is the latitudinal variation of the Coriolis parameter. They have been computed here using the values of λ_n from *Chelton et al.* [1998]. *Jacobs et al.* [2001] have taken $k = \frac{2\pi}{\alpha L_x^0}$ with $\alpha = 3$ to relate k to their e-folding length scale. A better way to determine α here is to use the energy spectrum E(k) described by *Arhan and Colin de Verdière* [1985] that corresponds to our covariance model.

The relation between $\langle k \rangle$ and L_x^0 is obtained by integrating the following function: $\langle k \rangle = \frac{\int kE(k)}{\int E(k)}\bigg|_{L_x^0}$. The solution is $\langle k \rangle = \frac{2\pi}{3.5 * L_x^0}$, $\alpha = 3.5$ (respectively $\langle l \rangle = \frac{2\pi}{3.5 * L_y^0}$).

[34] To compare the zonal propagation speeds of TPERS to the theoretical ones, we kept only the negative values of Cpx; this removed, in particular, the propagation velocities that mainly represent the effect of mean flow advection. In Figure 10, we compare the TPERS (crosses) and POP (diamonds) propagation speeds with the theoretical Rossby wave propagation speeds computed as defined above. The ratio of the propagation speeds observed/simulated to the theoretical ones is averaged for each band of 2°-latitude width between 10°N and 50°N.

[35] At latitudes lower than 28°N, the waves or eddies observed by TPERS propagate at speeds slightly faster than the theoretical speeds for non-infinite wavelengths. Between 28°N and 50°N, the propagation speeds observed are faster than the theoretical speeds by a factor of about 1.5. Observed and simulated speeds are thus significantly faster than the theoretical values. The difference is actually larger if we estimate the propagation speed from the slope of the maximum correlation axis of the space/time correlation matrix (which is the usual definition of propagation speed). Indeed, as was pointed out to us by D. Chelton and M. Schlax (personal communication, 2004), the Cpx derived from our covariance model do not correspond to the maximum correlation axis of the space/time correlation matrix. We have assumed that eddies, while propagating, decay over time (Gaussian damping term with an e-folding timescale of T); as a result, for a given spatial lag dx, the maximum correlation will be found for a time lag smaller
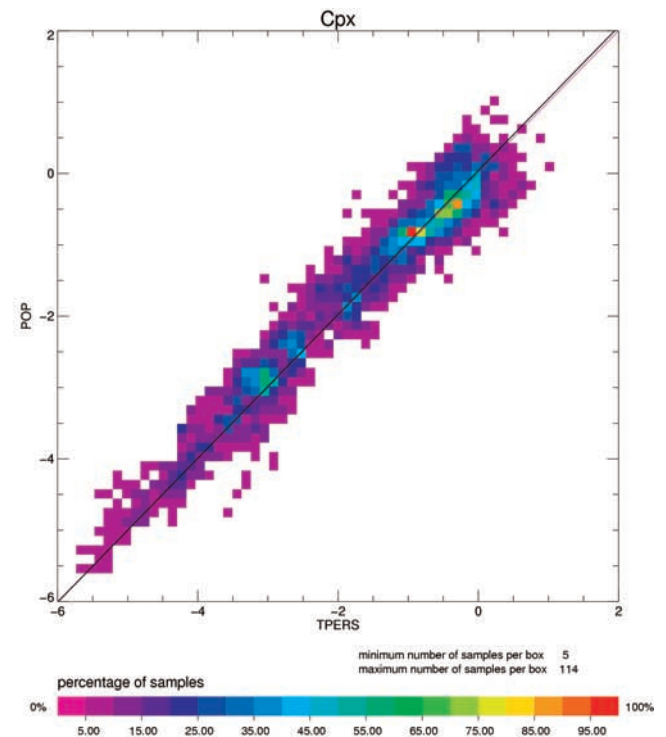
Figure 9. Scatterplot of the zonal propagation speed between POP and TPERS.
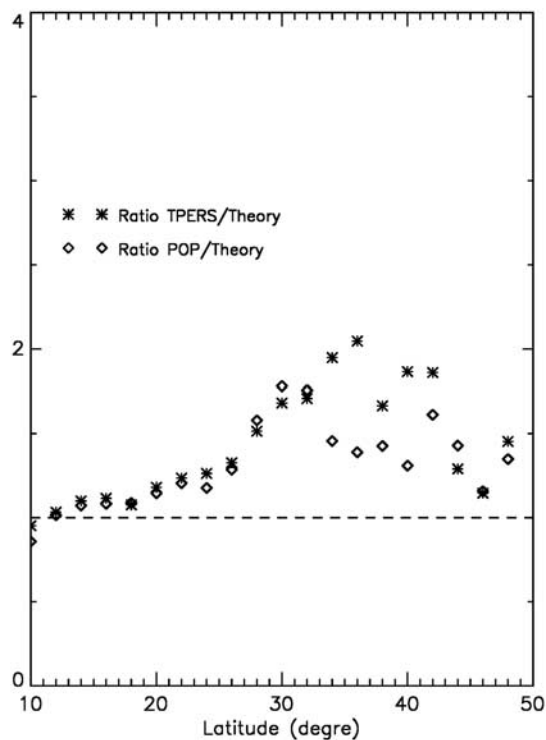
Figure 10. Ratio of observed propagation speed to theoretical speed for TPERS (crosses) and for POP (diamonds).

than dx/cpx. The speed derived from the tilt of the space/time covariance matrix will thus be faster than the estimation derived from our covariance model. This effect was quantified from our covariance parameters; that is, speeds are faster by a factor of 1.4 to 1.6 depending on latitude.

[36] *Chelton and Schlax* [1996] also found that the propagation speeds based on observations from T/P are higher than those given by linear theory. They were, however, dealing with long-wave (infinite) wavelengths. The major difference in the present study is that we are analyzing mesoscale signals (i.e., wavelengths below 500 km outside the tropical band) as per *Jacobs et al.* [2001]. However, eddies also seem to propagate at speeds higher than the standard Rossby wave theoretical values. Whether this reflects the effect of nonlinearities and/or the mechanism proposed by *Killworth et al.* [1997] is an open issue.

5. Time Variations of the EKE

5.1. Seasonal Variations of the EKE

[37] Several studies have been performed to characterize the seasonal variations of the mesoscale variability. In the work of *Ducet et al.* [2000], the seasonal signal explained a high percentage of the total EKE variance in several parts of the Global Ocean. Hereinafter, we describe the seasonal signal of the EKE in the North Atlantic computed from a 5-year-long time series of POP and TPERS data.

[38] On the basis of previous results, particular attention is paid to the wind stress role on the EKE seasonal signal. *White and Heywood* [1995] pointed out that the changes in eddy variability depend directly on forcing by wind stress in regions with a noticeable seasonal signal and on baroclinic

instability in regions of strong currents [see also *Stammer*, 1997; *Vivier et al.*, 1999; *Kelly et al.*, 1999]. In regions containing high mesoscale surface variability, *Garnier and Schopp* [1999] suggested that the mesoscale activity is intensified by the occurrence of a zonal wind induced geostrophic velocity. *Stammer and Wunsch* [1999] found a significant correlation between generation of EKE and wind stress forcing in the northern and eastern North Atlantic. *Stammer et al.* [2001] corroborates that conclusion in the weak-stratified regions of the northern North Atlantic Ocean.

5.1.1. Method

[39] At first, we apply a Loess low-pass time filter [*Schlax and Chelton*, 1992] to POP and TPERS SLA grids to keep low frequencies (over the period December 1992 to December 2000). By subtracting the low frequencies from the total signal, we keep only the high frequencies (HF) (that means here periods less than 200 days) while eliminating low frequencies such as the seasonal and the interannual variability of the ocean circulation. We then obtain the monthly HF-EKE by computing the geostrophic velocities. Note that "monthly" means a 3-month sliding average; for example, June is the average of May, June, and July in order to smooth the results.

[40] The phase φ and the amplitude A of the EKE annual signal are then computed by fitting a sinusoid with a period of 1 year. To help visualize and interpret φ and A, we compute the seasonal signal described by the following function: $f(t) = A\cos(\frac{2\pi t}{12} - \varphi)$ for t = 1, 3, 5, 7, 9 that correspond to January, March, May, July, September, and November. Figures 11 and 12 represent the seasonal signal of the high-frequency EKE for these different months, for, respectively, TPERS and POP. We then correlate the seasonal variations of the HF-EKE to the wind stress variations. The 6-hour wind stress fields from ECMWF are averaged monthly. Finally, the POP and TPERS HF-EKE and the wind stress are spatially averaged over different characteristic zones (see Figure 13). Those regions were chosen because the seasonal EKE signal represents a large portion of the total EKE variance.

5.1.2. Comparison of the EKE Seasonal Signal of POP and TPERS

5.1.2.1. High Latitudes

[41] The observations show a strong seasonal signal in high latitudes (more than 40% of the total signal). In the Labrador Sea, the signal is minimum in autumn (Figure 11 for TPERS). In early winter we can observe the appearance of a very small signal, then an increase in intensity during late winter/early spring close to the Greenland coasts, in the Labrador Sea and south of Iceland. The signal reaches its maximum in April. It then progressively decreases until August. The model is in good agreement with the annual cycle of TPERS at high latitudes (Figure 12), but with a time lag of 1 or 2 months compared to the observations. An interpretation is given in the next section.

5.1.2.2. Gulf Stream

[42] Figure 11 illustrates that the seasonal variations of the EKE occur in the whole Gulf Stream (the seasonal signal represents around 15% of the total signal), from its separation from the coast at Cape Hatteras up to the branching of the North Atlantic Current. The seasonal cycle of the EKE signal can be summarized in three steps: no
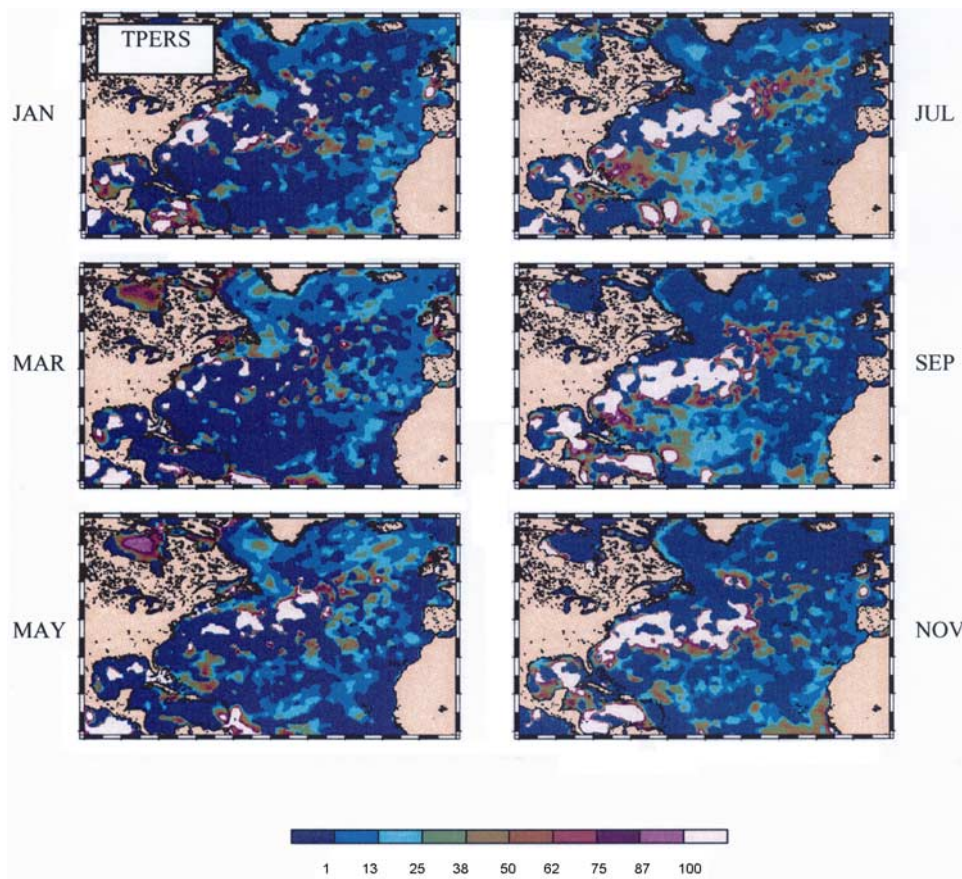
Figure 11. Evolution with time of the annual signal of the EKE for TPERS.

major signals in late winter, an increase of the signal until August/September, and then a decrease of the signal until January. The seasonal variations of the EKE in the model are less marked (Figure 12). We noted in section 3 that the model is error prone in simulating a realistic Gulf Stream, particularly close to 303°E, 35°N, where the variability is strongly reduced. The EKE seasonal cycle is accordingly less realistic.

5.1.2.3. Caribbean Sea

[43] The evolution of the variability in the model and the observations in the Caribbean Sea is well described in Figure 11 and in Figure 12. The seasonal signal in this region represents more than 60% of the total signal. For TPERS, we detect a maximum of the EKE seasonal cycle at 305°E and 10°N in March, off the Trinidad and Tobago shores, then this signal extends along the islands with a first maximum at 298°E (from the island of Grenada to the island of Dominica) and across the Lesser Antilles with a second maximum at 15°N. This patch is intensified from June to October to the west up to 285°E, whereas the other maximum of variability moves until August to the north, then decays progressively. The seasonal signal at 305°E and 10°N shows a time lag of 1 month with POP. This signal propagates in the same way as in TPERS and extends from 9°N to 14°N. The signal fades strongly after crossing the islands; it becomes more zonal, and narrow in latitude. Then it extends to the west until September/October. In August the signal expands to the north to Puerto Rico. The annual signal of variability is finally present in the whole Carib-

bean Sea in autumn and ends in November/December, except in Jamaica where the seasonal signal reaches its maximum in December and remains high during winter. The westward propagation of the variability is in good agreement with the results obtained by *Didden and Schott* [1993] and corresponds to the propagation of eddies coming from the retroflection region of the North-Brazil Current and directed toward the Caribbean Sea [*Carton and Chao*, 1999; *Ducet*, 2000].

5.1.3. Wind-Forcing and EKE Seasonal Variations

[44] Figure 13 shows the temporal evolution of the monthly means of the HF-EKE for POP (solid line) and for TPERS (dashed line), and the mean square wind stress τ^2 (dotted lines) averaged over four boxes: (1) the box between 34°N and 42°N, 295°E and 315°E, which represents a large part of the Gulf Stream, (2) the east of Greenland box: 55°N–64°N, 335°E–350°E, (3) the Caribbean Sea box: 12°N–17°N, 290°E–305°E, and (4) the Labrador Sea box: 55°N–63°N, 302°E–312°E. The constant value for TPERS between December 1993 and March 1995 corresponds to missing data of ERS-1/2. The values of τ^2 have been multiplied by 10^4. The unit is then 10^{-4} N/m^2.

[45] For the Gulf Stream box, Figure 13, the minimum (maximum) is observed in winter (summer) in phase opposition to the wind stress. The model follows the data with a correlation coefficient (CC) of 0.6 with a lead of 2 months. Note that the values of τ^2 have been multiplied by 2. The seasonal variations of the observed and simulated EKE have no direct relation to the seasonal cycle of the wind stress.
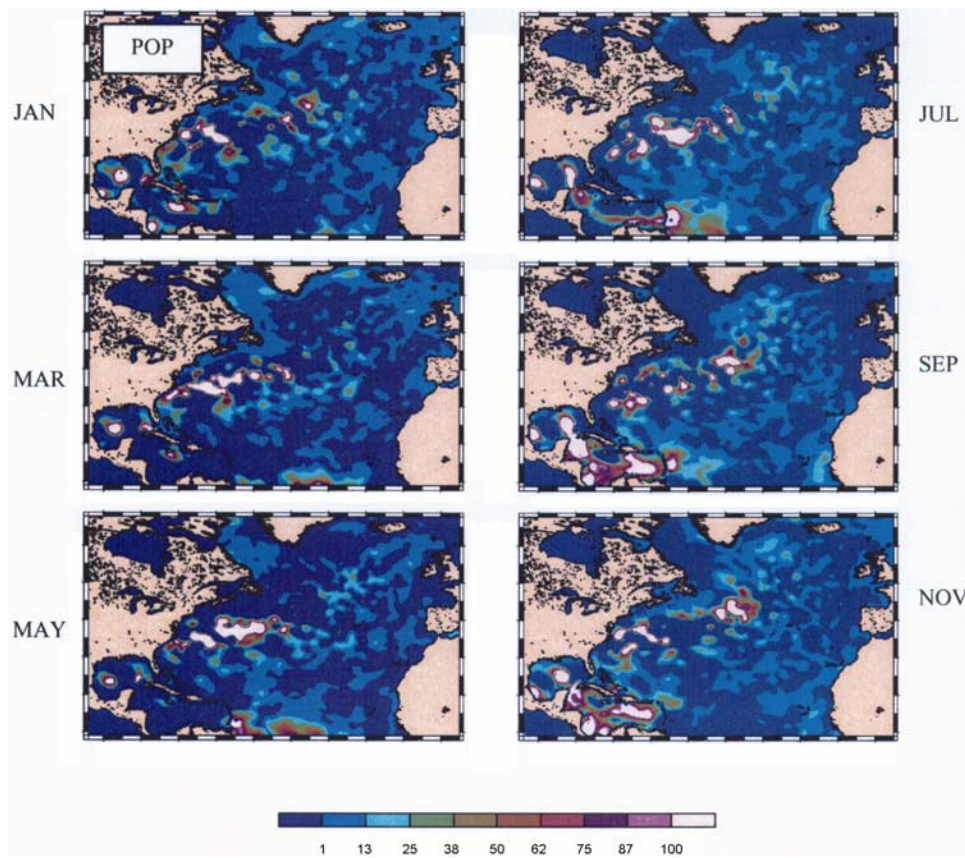
Figure 12. Evolution with time of the annual signal of the EKE for POP.

This is in agreement with findings of previous investigators who have obtained similar results in regions of high mesoscale variability [*Barnier et al.*, 2001; *Stammer et al.*, 2001; *White and Heywood*, 1995]. The hypothesis given by *Strass et al.* [1992] is that the seasonal variations of the mixed layer could be the reason for the seasonal variations of the variability of the Gulf Stream.

[46] As far as the signal south of Iceland is concerned, the maximum for the wind stress seasonal cycle is in January or February and March or April for TPERS. As described by *Stammer and Wunsch* [1999] and *Stammer et al.* [2001], the wind seems to lead the seasonal signal of the HF-EKE in that region. The seasonal cycle is lessened for POP. One reason for this difference between POP and TPERS is the percentage of the variance of EKE explained by the seasonal cycle in that region: more than 60–70% for TPERS and less than 50% for POP.

[47] For the Caribbean Sea, the model obtains the same characteristics as in the observations, except for 93 to 95. The study of the EKE with time (Figure 13) in the Caribbean Sea reveals the above discussed marked seasonal cycle for both POP and TPERS with a noticeable lag of 2 months for the model.

[48] In the Labrador Box, there is a quasi-sinusoidal EKE signal for TPERS and POP that appears to be strongly correlated to the wind stress (values divided by 10) (Figure 13). The good agreement in both amplitude and variations between POP and TPERS is noticeable (especially in the year 1996) with a global coefficient of correlation (CC) of 0.71 (and no time lag), and between TPERS and τ^2

with a CC of 0.80 for a 2-month phase lag. The small variations of the wind stress, like, for example, in November 1996, are found in TPERS in January 1997, 2 months later.

[49] Our results follow *White and Heywood* [1995], *Garnier and Schopp* [1999], *Stammer and Wunsch* [1999], and *Stammer et al.* [2001], which link seasonal EKE variations to seasonal wind stress variations. However, more recently, *Eden and Böning* [2002] explained the seasonal variations of the eddy field by a seasonally modulated instability of the West Greenland Current and not by a direct forcing of high-frequency wind variations. The exact mechanisms of EKE seasonal variations in the different part of the North Atlantic Ocean described here are not yet well known. The different hypothesizes need to be considered and confirmed with three-dimensional-data model outputs.

[50] Others regions show significant EKE seasonal variations.

[51] The amplitude of the seasonal signal in the Canary Current represents more than 60% (70% for POP) of the EKE total variance. The variability is highest in autumn as shown in Figure 11, which was described already in previous studies [*Arístegui et al.*, 1994]. The intensification of the trade wind during summer accelerates the Canary Current and creates an area of variability during autumn due to instabilities of the Canary Current as it crosses the archipelago and due to the wind stress curl forcing downstream from the islands [*Le Traon and Morrow*, 2001].

[52] Close to the coast of Mauritania, there is a noticeable seasonal cycle accounting for more than 50% of the EKE total variance. The maximum of the signal is detected at
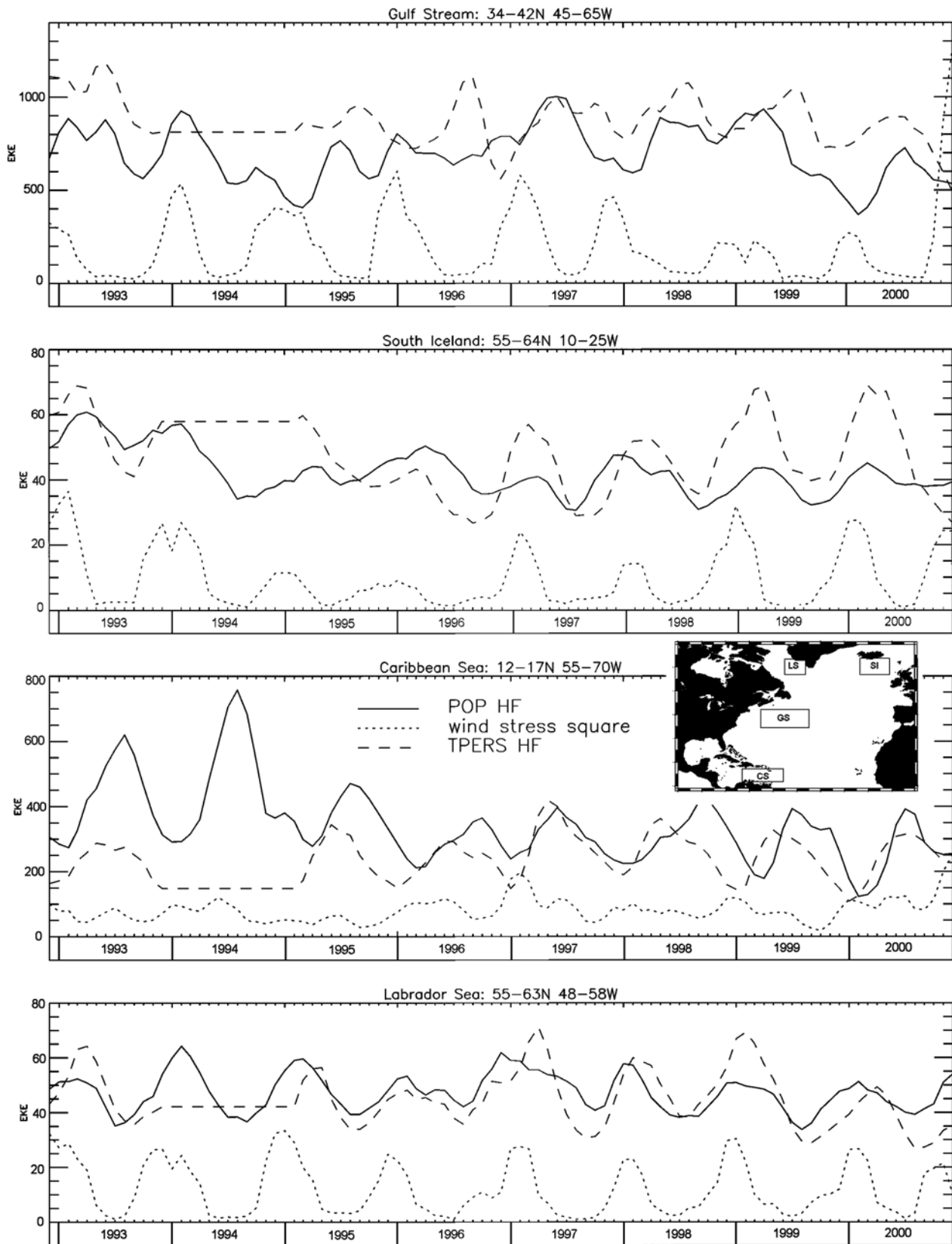
Figure 13. Monthly averaged EKE for POP (solid line), TPERS (dashed line), and the wind stress square (dotted line) in the Gulf Stream, GS, the Labrador Sea, LS, the Iceland Basin, SI, and the Caribbean Sea, CS. EKE is in cm^2/s^2; the unit of the wind stress is 10^{-4} N/m^2. The values of the wind stress have been multiplied by 2 in the Gulf Stream box and divided by 10 in the South Iceland and Labrador Sea boxes.
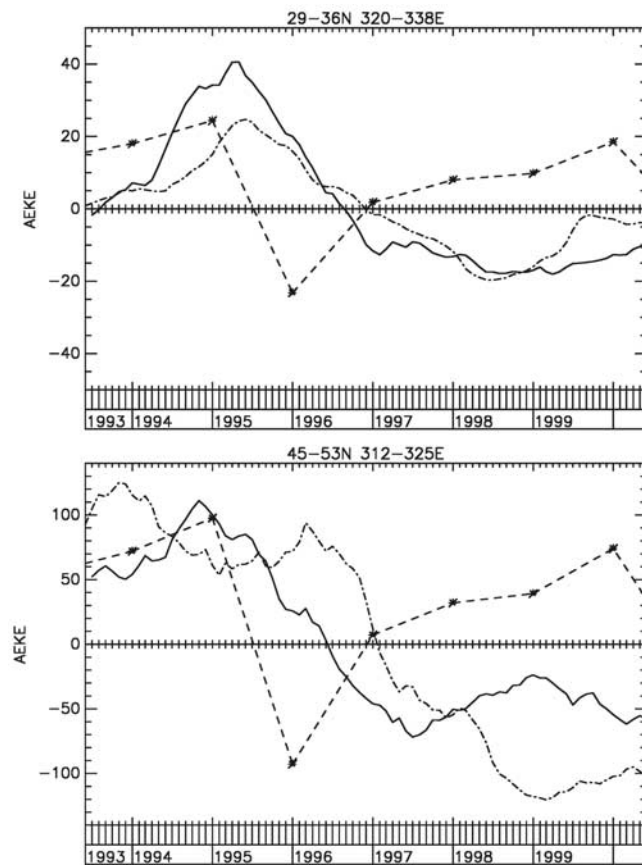
Figure 14. Monthly averaged anomalies of EKE for POP (dash-dotted line), TPERS (solid line), and the North Atlantic Oscillation (dotted line) (top) in the Azores Current (29°N–36°N, 320°E–338°E and (bottom) in the Newfoundland Basin (45°N–53°N, 312°E–325°E).

the end of the summer in the model and during autumn in the observations. This signal is directly linked to the upwelling that occurs during the trade wind intensification in summer.

5.2. Interannual Variability

[53] Our data sets allow us to study the HF-EKE interannual variability over 8 years in the North Atlantic Ocean and to measure the possible influence of a major climatic event such as the North Atlantic Oscillation (NAO). *Stammer and Wunsch* [1999] first pointed out an interannual variability of the EKE between the years 1993 and 1996 and noticed an eventual link between the EKE and the NAO Index. This approach is quite new, as the long-term variations of the HF-EKE in the North Atlantic are little known today.

[54] The annual means of the HF-EKE anomalies for TPERS and POP were first computed and compared over the North Atlantic (not shown). First, as expected, the interannual variability is well marked in the Gulf Stream. *Volkov* [2004] found, for example, a 2°-southward shift of the EKE in the Gulf Stream 2 years after the sign change of the NAO Index. This effect is not observed, however, in the POP simulation. We focus on two regions that seem to present a similar interannual variability in both data and

model: in the Azores Current (AC) and above the New-foundland basin, in the North Atlantic Drift (NAD). To better characterize these variations, in Figure 14, we show the EKE anomalies for these particular two regions, in the AC box: 26°N–36°N, 320°E–338°E and in the NAD box: 45°N–53°N, 312°E–325°E. To estimate the interannual signal, we applied a running mean with a window width equal to 13 months (6 months before and after the month in progress) and compared it to the NAO Index, [*Hurrel*, 1995], a dominant mode of the atmospheric processes over the North Atlantic. The data between December 1993 and March 1995 correspond to the TP EKE data multiplied by a factor equal to the ratio between TPERS and TP EKE over their common time period.

[55] The change of sign of the HF-EKE anomalies occurs at the end of 1996 in the AC and in the NAD for both TPERS and POP. For the NAD, the model follows the observations with a larger amplitude; since the model is more turbulent in that part of the ocean, the anomalies are expected to be larger there.

[56] All these changes took place in 1996, the year of a change sign of the NAO index. Actually, in 1996, the NAO index becomes negative, which corresponds to a decrease of the westerly winds. Recently, *Volkov and van Aken* [2003] and *Esselborn and Eden* [2001] analyzed the SLA interannual variability with 8 years of altimetric data. They found a significant correlation coefficient between the annually averaged SLA and the North Atlantic Oscillation (NAO) Index. The first empirical orthogonal function (EOF) of the SLA shown by *Esselborn and Eden* [2001] reveal a basin scale dipole between the subtropical and subpolar gyre. During high NAO, the two gyres are highly visible with an intensification of the cyclonic circulation in the subpolar gyre and of the anticyclonic circulation in the subtropical gyre. *Bersch* [2002], using hydrographic data, suggested a contraction of the subpolar gyre (i.e., NAC and NAD) during negative NAO (in 1996 and 1997) and found that the cyclonic circulation is then reduced. In parallel, because of the existence of the dipole, the subtropical gyre (i.e., AC) height decreases and the circulation is also reduced. The circulation should then be less turbulent and should generate less mesoscale activity (Figure 14). *Volkov and Aken* [2003] noted that the sea responds to the changes in the NAO index within 1 year. *Reverdin et al.* [1999] found a significant increase of the sea level in the subpolar gyre between October and December 1996. It seems here that the eddy activity reacts to an interannual change of the atmosphere during the following year: late summer in the Azores Current for TPERS and in the beginning of 1997 for POP, early summer in the Newfoundland Basin for TPERS and in the beginning of 1997 for POP. *Penduff et al.* [2003] found a relationship between strong NAO events and gyre-scale EKE fluctuations with a 4- to 12-month lag. The adjustment of the ocean circulation to the NAO plus the time for the instabilities to grow would thus imply a time response of the EKE around 1 year. This should be analyzed further with much longer time series (high-resolution model simulations with many realizations of the NAO).

[57] In the Caribbean Sea the model has a very strong interannual signal with two maxima in positive anomalies, in 1994 and in 1997. We find the same maximum in the observations but not as strong. *Murphy et al.* [1999] found
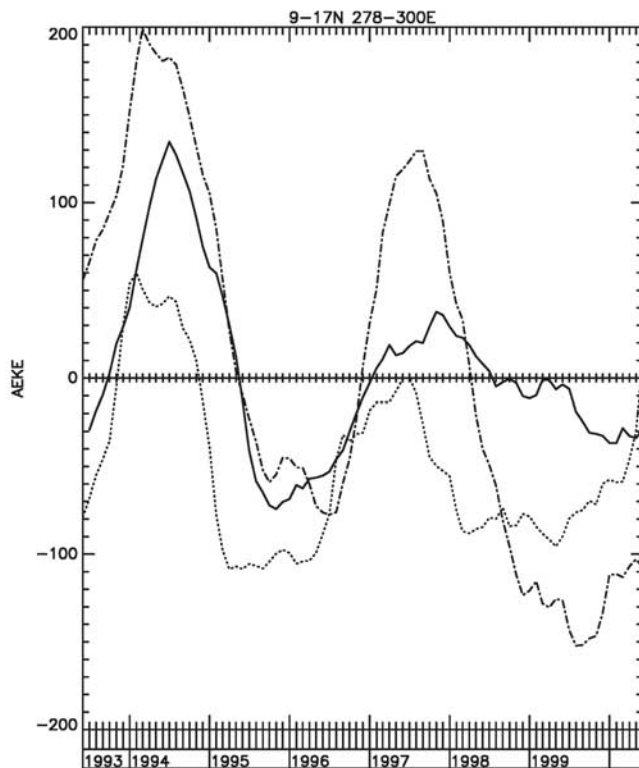
Figure 15. Monthly averaged anomalies of EKE for POP (dash-dotted line), TPERS (solid line), and the anomalies of wind stress square (dotted lines) in the Caribbean Sea (9°N–17°N, 278°E–300°E).

with their numerical simulations that the interannual variability of the SLA during the 1990s was due to an anomaly in the wind field over the basin. In Figure 15 the anomalies of wind stress square are plotted. The maximum seems to be approximately 5 months before the maximum of TPERS and 2 months before the maximum of POP. We did not find a significant interannual variability in the region of eddies generated by the retroflexion of the NECC. It is thus likely that the observed interannual variability is due to the wind-forcing following the hypothesis of *Murphy et al.* [1999]. The mechanism would thus be very different from the one that explains the seasonal EKE variations.

6. Conclusion

[58] The objective of the paper was to analyze the degree of realism of the POP model using T/P and ERS altimeter data and to describe the mesoscale activity in the North Atlantic Ocean. The comparison of the mean EKE (1995–2000) between the POP model outputs and combined altimeter data sets from TP and ERS shows the remarkable progress made in relation to previous model studies with lower-resolution models [*Chao and Fu*, 1995; *Chao et al.*, 1996]. However, the model needs to be improved in the Gulf Stream area where it is too energetic between Cape Hatteras and the Corner Rise Seamounts.

[59] The agreement of the characteristic space and time-scales of mesoscale variability derived from altimetry and the LANL model is encouraging. The spatial scales match

accurately and decrease as expected because of the north-ward decrease of the first baroclinic Rossby radius of deformation. Propagation velocities are also in close agreement. The effect of mean flow advection is clearly seen in both model and altimeter data. A comparison with standard Rossby wave theory shows that eddies propagate faster than non infinite Rossby waves by a factor of 1.5 to 2. The major difference between our work and previous studies is that our results are mainly representative of mesoscale eddies (wavelengths below 500 km) while previous studies such as that of *Chelton et al.* [1998] were analyzing long Rossby waves.

[60] The temporal evolution of the monthly EKE over the 8-year period (from December 1992 to December 2000) has been compared with the wind stress in several selected regions. Our results follow *White and Heywood* [1995], *Garnier and Schopp* [1999], and *Stammer et al.* [2001], which link seasonal EKE variations to seasonal wind stress variations even if the question is still widely open as recently discussed by *Eden and Böning* [2002]. The exact mechanisms of EKE seasonal variations in the different parts of the North Atlantic Ocean described here is not yet well known.

[61] An EKE interannual variability in the major currents of the different gyres has been shown. Previous studies pointed out the role of the NAO sign change on the ocean circulation, with a reduction of the intensity of the circulation during negative NAO [*Bersch*, 2002; *Curry and McCartney*, 2001]. We hypothesize that a reduction of this intensity could entertain a decrease of the eddy activity along the branch of the subpolar and subtropical gyres.

References

Arhan, M., and A. Colin de Verdiere (1985), Dynamics of eddy motions in the eastern North Atlantic, *J. Phys. Oceanogr.*, *15*, 153–170.
Arístegui, J. P., S. Sangrá, Hernández-león, M. A. Cantón, Hernández-Guerra, and J. L. Kerling (1994), Island eddies in the Canary Islands, *Deep Sea Res.*, *41*, 1509–1525.
Barnier, B., L. Siefridt, and P. Marchesiello (1995), Thermal forcing for a global ocean circulation model using a three-year climatology of ECMWF analyses, *J. Mar. Syst.*, *6*, 363–380.
Barnier, B., T. Reynaud, A. Beckmann, C. Böning, J.-M. Molines, S. Barnard, and Y. Jia (2001), On the seasonal variability and eddies in the North Brazil Current: Insights from model intercomparison experiments, *Prog. Oceanogr.*, *48*, 195–230.
Bersch, M. (2002), North Atlantic Oscillation–induced changes of the upper layer circulation in the northern North Atlantic Ocean, *J. Geophys. Res.*, *107*(C10), 3156, doi:10.1029/2001JC000901.
Carton, J. A., and Y. Chao (1999), Caribbean Sea eddies inferred from TOPEX/Poseidon altimetry and a 1/6° Atlantic Ocean model simulation, *J. Geophys. Res.*, *104*(C4), 7743–7752.
Chao, Y., and L.-L. Fu (1995), A comparison between the TOPEX/Poseidon data and a global ocean general circulation model during 1992–1993, *J. Geophys. Res.*, *100*(C12), 24,965–24,976.
Chao, Y., A. Gangopadhyay, F. O. Bryan, and W. R. Holland (1996), Modeling the Gulf Stream system: How far from reality?, *Geophys. Res. Lett.*, *23*, 3155–3158.
Chelton, D. B., and M. G. Schlax (1996), Global observations of oceanic Rossby waves, *Science*, *272*, 234–238.
Chelton, D. B., R. A. DeSzoeke, M. G. Schlax, K. El Naggar, and N. Siwertz (1998), Geographical variability of the first baroclinic Rossby radius of deformation, *J. Phys. Oceanogr.*, *28*, 433–460.

Curry, R. G., and M. S. McCartney (2001), Ocean gyre circulation changes associated with the North Atlantic Oscillation, *J. Phys. Oceanogr.*, *31*, 3374–3400.

Cushman-Roisin, B. C., E. P. Chassignet, and B. Tang (1990), Westward motion of mesoscale eddues, *J. Phys. Oceanogr.*, *20*, 758–768.

Didden, N., and F. Schott (1993), Seasonal variations in the western tropical Atlantic: Surface circulation from Geosat altimetry and WOCE model results, *J. Geophys. Res.*, *97*(C3), 2541–3529.

Ducet, N. (2000), Combinaison des données altimétriques TOPEX/Poseidon et ERS-1/2 pour l'étude de la variabilité mesoéchelle: Comparaison avec un modèle à haute résolution de l'Atlantique Nord, Ph.D. thesis, Paul Sabatier Univ., Toulouse, France.

Ducet, N., and P.-Y. Le Traon (2001), A comparison of surface eddy kinetic energy and Reynolds stresses in the Gulf Stream and the Kuroshio Current systems from merged TOPEX/Poseidon and ERS-1/2 altimetric data, *J. Geophys. Res.*, *106*(C8), 16,603–16,622.

Ducet, N., P.-Y. Le Traon, and G. Reverdin (2000), Global high resolution mapping of ocean circulation from TOPEX/Poseidon and ERS-1/2, *J. Geophys. Res.*, *105*(C5), 19,477–19,498.

Eden, C., and C. Böning (2002), Sources of eddy kinetic energy in the Labrador Sea, *J. Phys. Oceanogr.*, *32*, 3346–3363.

Esselborn, S., and C. Eden (2001), Sea surface height changes in the North Atlantic Ocean related to the North Atlantic Oscillation, *Geophys. Res. Lett.*, *28*, 3473–3476.

Frankignoul, C., and P. Müller (1979), Quasi-geostrophic response of an infinite beta-plane ocean to stochastic forcing by atmosphere, *J. Phys. Oceanogr.*, *9*, 104–127.

Fratantoni, D. M. (2001), North Atlantic surface circulation during the 1990s observed with satellite-tracked drifters, *J. Geophys. Res.*, *106*(C10), 22,067–22,093.

Garnier, V., and R. Schopp (1999), Wind influence on the mesoscale activity along the Gulf Stream and the North Atlantic currents, *J. Geophys. Res.*, *104*, 18,087–18,110.

Holland, W. R., P. E. Harrison, and A. J. Semtner (1982), Eddy resolving numerical models of large-scale ocean circulation, in "*Eddies in Marine Science*," edited by A. R. Robinson, pp. 545–562, Springer-Verlag, New York.

Hurlburt, H. E., and P. J. Hogan (2000), Impact of 1/8° to 1/64° resolution on Gulf Stream model-data comparisons in basin-scale subtropical Atlantic Ocean models, *Dyn. Atmos. Oceans*, *32*, 283–329.

Hurrel, J. W. (1995), Decadal trends in the North Atlantic Oscillation: Regional temperatures and precipitation, *Science*, *269*, 676–679.

Jacobs, G. A., C. N. Barron, and R. C. Rhodes (2001), Mesoscale characteristics, *J. Geophys. Res.*, *106*(C9), 19,581–19,595.

Kelly, K. A., S. Singh, and R. X. Huang (1999), Seasonal variations of sea surface height in the Gulf Stream region, *J. Phys. Oceanogr.*, *29*, 313–327.

Killworth, P. D., D. B. Chelton, and R. A. DeSzoeke (1997), The speed of observed and theoretical long extratropical planetary waves, *J. Phys. Oceanogr.*, *27*, 1946–1966.

Kuragano, T., and M. Kamachi (2000), Global statistical space-time scales of oceanic variability estimated from the TOPEX/Poseidon altimeter data, *J. Geophys. Res.*, *105*(C1), 955–974.

Larnicol, G. (1998), Analyse de la variabilité de l'Océan Atlantique à partir des données altimétriques TOPEX/Poseidon et d'un modèle inverse non linéaire, Ph.D. thesis, Occidental Britanny Univ., Brest, France.

Le Traon, P.-Y. (1991), Time scales of mesoscale variability and their relationship with space scales in the North Atlantic, *J. Mar. Res.*, *49*, 467–492.

Le Traon, P.-Y., and G. Dibarboure (2002), Velocity mapping capabilities of present and future altimeter missions: The role of high frequencies signals, *J. Atmos. Oceanic Technol.*, *19*, 2077–2088.

Le Traon, P.-Y., and R. Morrow (2001), Ocean currents and eddies, in *Satellite Altimetry and Earth Sciences*, edited by L.-L. Fu and A. Cazenave, pp. 171–215, Academic, San Diego, Calif.

Levitus, S. (1982), Climatological atlas of the world ocean, *NOAA Prof. Pap. 13*, 173 pp., Natl. Oceanic and Atmos. Admin., Silver Spring, Md.

Lozier, M. S. (1997), Evidence for large-scale eddy-driven gyres in the North Atlantic, *Science*, *277*, 361–364.

McClean, J. L., A. J. Semtner, and V. Zlotnicki (1997), Comparisons of mesoscale variability in the Semtner-Chervin 1/4° model, the Los Alamos Parallel Ocean Program 1/6° model, and TOPEX/Poseidon data, *J. Geophys. Res.*, *102*(C11), 25,203–25,226.

McWilliams, J. C., and G. R. Flierl (1979), On the evolution of isolated, nonlinear vortices, *J. Phys. Oceanogr.*, *9*, 1155–1182.

Murphy, S. J., H. E. Hurlburt, and J. J. O'Brien (1999), The connectivity of eddy variability in the Caribbean Sea, the Gulf of Mexico, and the Atlantic Ocean, *J. Geophys. Res.*, *104*(C1), 1431–1453.

Nof, D. (1981), On the beta-induced movement of isolated baroclinic eddies, *J. Phys. Oceanogr.*, *11*, 1662–1672.

Pacanowski, R. C., and S. G. H. Philander (1981), Parameterization of vertical mixing in numerical models of tropical oceans, *J. Phys. Oceanogr.*, *11*, 1443–1451.

Pedlosky, J. (1987), *Geophysical Fluid Dynamics*, 710 pp., Springer-Verlag, New York.

Penduff, T., B. Barnier, W. K. Dewar, and J. J. O'Brien (2003), Dynamical response of the oceanic eddy field to the North Atlantic Oscillation: A model-data comparison, *J. Phys. Oceanogr.*, in press.

Reverdin, G., N. Verbrugge, and H. Valdimarsson (1999), Upper ocean variability between Iceland and Newfoundland, 1993–1998, *J. Geophys. Res.*, *104*(C12), 29,599–29,611.

Roemmich, D., and J. Gilson (2001), Eddy transport of heat and thermocline waters in the North Pacific: A key to interannual/decadal climate variability?, *J. Phys. Oceanogr.*, *31*, 675–687.

Schlax, M. G., and D. B. Chelton (1992), Frequency domain diagnostics for linear smoothers, *J. Am. Stat. Assoc.*, *87*, 420.

Smith, R. D., M. E. Maltrud, F. O. Bryan, and M. W. Hecht (2000), Numerical simulation of the North Atlantic Ocean at 1/10°, *J. Phys. Oceanogr.*, *30*, 1532–1561.

Stammer, D. (1997), Steric and wind-induced changes in TOPEX/Poseidon large-scale sea surface topography observations, *J. Geophys. Res.*, *102*(C9), 20,987–21,009.

Stammer, D., and C. Wunsch (1999), Temporal changes in eddy energy of the oceans, *Deep Sea Res.*, *46*, 77–108.

Stammer, D., R. T. Tokmakian, A. Semtner, and C. Wunsch (1996), How well does a 1/4° global circulation model simulate large-sale oceanic observations?, *J. Geophys. Res.*, *101*(C11), 25,779–25,811.

Stammer, D., C. Böning, and C. Dieterich (2001), The role of variable wind forcing in generating eddy energy in the North Atlantic, *Prog. Oceanogr.*, *48*, 289–311.

Strass, V. H., H. Leach, and J. D. Woods (1992), On the seasonal development of mesoscale variability: The influence of the seasonal pycnocline formation, *Deep Sea Res.*, *29*, 1627–1639.

Thompson, L., K. A. Kelly, D. Darr, and R. Hallberg (2002), Buoyancy and mixed layer effects on the sea surface height response in an isopycnal model of the North Pacific, *J. Phys. Oceanogr.*, *32*, 3657–3670.

Vivier, F., K. A. Kelly, and L. Thompson (1999), Contribution of wind forcing, waves, and surface heating to sea surface height observations in the Pacific Ocean, *J. Geophys. Res.*, *104*(C9), 20,767–20,788.

Volkov, D. L. (2004), The interannual variability of the altimetry-derived eddy field and associated surface circulation in the North Atlantic Ocean in 1993–2001, *J. Phys. Oceanogr.*, in press.

Volkov, D. L., and H. M. van Aken (2003), Annual and interannual variability of sea level in the northern North Atlantic Ocean, *Journal of Geophysical Research*, *108*(C6), 3204, doi:10.1029/2002JC001459.

White, M. A., and K. Heywood (1995), Seasonal and interannual changes in the North Atlantic subpolar gyre from Geosat and TOPEX/Poseidon altimetry, *J. Geophys. Res.*, *100*(C12), 24,931–24,941.

Wunsch, C. (1999), Where does ocean eddy heat fluxes matter?, *J. Geophys. Res.*, *104*(C6), 13,235–13,249.

Zang, X., and C. Wunsch (1999), The observed dispersion relationship for North Pacific Rossby wave motions, *J. Phys. Oceanogr.*, *29*, 2183–2190.

————————

S. Brachet and P. Y. Le Traon, CLS, Space Oceanography Division, 8-10 Rue Hermes, Ramonville-St-Agne F-31526, France. (sbrachet@cls.fr)